University of Reading

A comprehensive analysis of coherent rainfall patterns in China and potential drivers. Part II: intraseasonal variability

Article

Published Version

Creative Commons: Attribution 4.0 (CC-BY)

Open Access

Stephan, C. C., Klingaman, N. P., Vidale, P. L., Turner, A. G., Demory, M.-E. and Guo, L. (2017) A comprehensive analysis of coherent rainfall patterns in China and potential drivers. Part II: intraseasonal variability. Climate Dynamics. ISSN 0930-7575 doi: https://doi.org/10.1007/s00382-017-3904-6 Available at http://centaur.reading.ac.uk/72355/

It is advisable to refer to the publisher's version if you intend to cite from the work.

To link to this article DOI: http://dx.doi.org/10.1007/s00382-017-3904-6

Publisher: Springer

All outputs in CentAUR are protected by Intellectual Property Rights law, including copyright law. Copyright and IPR is retained by the creators or other copyright holders. Terms and conditions for use of this material are defined in the End User Agreement.

www.reading.ac.uk/centaur

University of Reading

CentAUR

Central Archive at the University of Reading

Reading's research outputs online

Clim Dyn
DOI 10.1007/s00382-017-3904-6

A comprehensive analysis of coherent rainfall patterns in China and potential drivers. Part II: intraseasonal variability

Claudia Christine Stephan[1] · Nicholas P. Klingaman[1] · Pier Luigi Vidale[1] · Andrew G. Turner[1,2] · Marie-Estelle Demory[1,3] · Liang Guo[1]

Received: 6 February 2017 / Accepted: 6 September 2017
© The Author(s) 2017. This article is an open access publication

Abstract The causes of subseasonal precipitation variability in China are investigated using observations and reanalysis data for extended winter (November–April) and summer (May–October) seasons from 1982 to 2007. For each season, the three dominant regions of coherent intraseasonal variability are identified with Empirical Orthogonal Teleconnection (EOT) analysis. While previous studies have focused on particular causes for precipitation variability or on specific regions, here a comprehensive analysis is carried out with an objective method. Furthermore, the associated rainfall anomaly timeseries are tied to specific locations in China, which facilitates their interpretation. To understand the underlying processes associated with spatially coherent patterns of rainfall variability, fields from observations and reanalysis are regressed onto EOT timeseries. The three dominant patterns in winter together explain 43% of the total space–time variance and have their origins in midlatitude disturbances that appear two pentads in advance. Winter precipitation variability along the Yangtze River is associated with wave trains originating over the Atlantic and northern Europe, while precipitation variability in southeast China is connected to the Mediterranean storm track. In summer, all patterns have a strong relationship with the Boreal Summer Intraseasonal Oscillation and are modulated by the seasonal cycle of the East Asian summer monsoon. The wet and dry phases of the regional patterns can substantially modulate the frequency of daily rainfall across China. The discovered links between weather patterns, precursors, and effects on local and remote precipitation may provide a valuable basis for hydrological risk assessments and the evaluation of numerical weather prediction models.

1 Introduction

Precipitation over China has a strong seasonal cycle, governed primarily by the East Asian Monsoon (EAM). The EAM is characterized by a distinct seasonal reversal of flow associated with sea-level pressure and temperature differences between the Asian continent and surrounding oceans (Webster et al. 1998; Chang 2004; Wang 2006). Therefore, the annual cycle of the EAM can be divided into a warm, wet summer monsoon and a dry, cold winter monsoon. In this study we define extended winter as November–April and extended summer as May–October.

The East Asian winter monsoon features strong northeasterly winds that transport dry and cold air from Siberia into China. On shorter timescales, East Asia is influenced both by midlatitude and tropical disturbances, due to its location in the subtropics. Extratropical systems affect weather extremes over China predominantly during winter. Cold surges are accompanied by strong winds and a sudden fall of surface air temperatures in the midlatitudes and subtropics (Boyle and Chen 1987), which can cause large damages from blizzards, freezing rain and low temperatures (Gu et al. 2008; Zhou et al. 2011; Wang et al. 2008; Gao et al. 2008).

The East Asian summer monsoon is characterized by strong southwesterlies that transport moisture into East Asia. Strong rainfall variability can produce disastrous regional

✉ Claudia Christine Stephan
c.c.stephan@reading.ac.uk

[1] National Centre for Atmospheric Science-Climate, Department of Meteorology, University of Reading, Reading, UK

[2] Department of Meteorology, University of Reading, Reading, UK

[3] Center for Space and Habitability, University of Bern, Gesellschaftsstrasse 6, 3012 Bern, Switzerland

Published online: 15 September 2017

droughts or floods (Huang et al. 1998; Huang and Zhou 2002; Barriopedro et al. 2012). During summer the tropical intraseasonal oscillation (ISO) is the dominant source of variability in the EAM [e.g., Webster et al. 1998]. In contrast to boreal winter, when the ISO is tropically confined and mainly eastward propagating, the boreal summer ISO (BSISO) extends further north. Both are manifestations of the Madden-Julian oscillation (MJO; Madden and Julian 1972). Lee et al. (2013) defined two indices for the extended boreal summer (May–October) ISO, which will be used in this study. The BSISO-1 index describes northward/northeastward propagation over the Indian summer monsoon region (Yasunari 1979, 1980; Krishnamurti and Subramanian 1982; Lau and Chan 1986; Wang et al. 2005; Annamalai and Sperber 2005) and northward/northwestward propagation over the Western North Pacific–East Asian region (Murakami 1984; Chen and Chen 1993; Kemball-Cook and Wang 2001; Kajikawa and Yasunari 2005; Yun et al. 2009, 2010); the BSISO-2 index also describes similar propagation in the Indian and Western North Pacific–East Asian sectors. However, the spatial structures of the circulation anomalies associated with BSISO-1 and BSISO-2 are different. In contrast to BSISO-1, convection associated with BSISO-2 first appears in the equatorial Indian Ocean and the Philippine Sea, and propagates northwestward over the Indian subcontinent as well as over the Western North Pacific–East Asian region. The northward propagating Rossby-wave like circulation patterns associated with BSISO-1 have periods of 30–60 days. BSISO-2 captures frontal-like systems with a southwest to northeast slope and periods of 10–30 days. While variability related to BSISO-1 occurs throughout May–October, that associated with BSISO-2 peaks during the monsoon onset season from late May to early July.

The impact of specific phenomena on precipitation in the EAM region has been investigated, e.g. cold surges (Lau and Lau 1984; Chen et al. 2004; Jeong and Ho 2005; Jeong et al. 2005, 2006), high-frequency synoptic variability (Hong 2004; Kim et al. 2010), mid- and high-latitude blocking (Wang et al. 2000; Samel and Liang 2003; Yihui and Chan 2005; Yang and Zhai 2014), and variability of the Arctic Oscillation (Wen et al. 2009; Mao et al. 2011). Modes of intraseasonal variability have been investigated for specific regions, e.g. for the southern and central portions of the Yangtze river basin (Yang et al. 2010; Mao and Wu 2006). The effect of the BSISO on precipitation in China has been described for specific regions and for individual rainfall events (e.g. Yang and Li 2003; Zhu et al. 2003; Mao et al. 2010; Gao et al. 2013; Liu et al. 2014; Li et al. 2015; Hsu et al. 2016). Previous studies have also linked subseasonal wintertime precipitation variability to the MJO (Liu and Yang 2010; Jia et al. 2011; He et al. 2011). Even though the MJO is the dominant mode of tropical subseasonal variability, Yao et al. (2015) showed in their Empirical Orthogonal Function (EOF) analysis of November–March pentad precipitation that the MJO is only relevant to South China, where in some locations it explains up to 10% of the subseasonal precipitation variability.

In this study we objectively determine coherent spatial patterns of intraseasonal rainfall variability, instead of relying on predefined regions or standard correlation analysis. Empirical Orthogonal Teleconnection analysis (EOT) is applied to observed precipitation from the APHRODITE data set. We also use EOT analysis and APHRODITE in Part I of this study (Stephan et al. 2017), where the focus is on interannual variability of seasonal precipitation. In Part I, EOT analysis successfully reproduces robust known patterns reported by several earlier studies; it also provides new insights into patterns of coherent precipitation variability and their causes. This study examines interannual and intraseasonal precipitation variability in China across all seasons, using the same technique.

The paper is arranged as follows. Section 2 introduces data sets and analysis techniques. Section 3 describes the leading patterns for wintertime subseasonal precipitation variability; Sect. 4 describes those for summer. Section 5 is a discussion; a summary of the main results is given in Sect. 6.

2 Data and methods

2.1 Empirical orthogonal teleconnections

In the following we will summarize the EOT analysis technique. Please refer to Part I for a detailed description of the method.

EOT analysis identifies independent regional patterns of variability (Van den Dool et al. 2000; Smith 2004). The EOT method has been successfully demonstrated for interannual precipitation variability (Smith 2004; Rotstayn et al. 2010; Klingaman et al. 2013; King et al. 2014) and for intraseasonal extreme precipitation (King et al. 2014). In Part I of this study (Stephan et al. 2017) the method was shown to successfully reproduce known patterns of interannual precipitation variability in China. Restricting our analysis domain to China, the first EOT is defined as the timeseries at the point that explains the most variance in the area-averaged precipitation timeseries. The associated spatial pattern is a map of correlation coefficients at each point with this so-called base point. To compute the second EOT timeseries, the first EOT timeseries is removed from all points in the domain by linear regression, and the above steps are repeated. The process can be repeated as many times as there are gridpoints.

EOT analysis thus identifies regions in which subseasonal precipitation varies strongly and coherently. Because

the EOT timeseries are constrained to be orthogonal only in time, not in space, it is possible to find more than one physical mechanism to be associated with precipitation in the same area.

As a measure of uncertainty due to a limited sample size in time, we compute the percentage of total explained space–time variance for each EOT leaving out 1 year at a time. If the difference between the greatest and smallest values is greater than half the difference between the total explained variance of an EOT and that of either of its neighbours, we consider the EOT to be degenerate. The fractions of total space–time variance explained by the seven leading EOTs for winter and summer are shown in Fig. 1. In summer, the first four EOTs are distinct from the others. In winter, EOTs 1, 2 and 3 are distinct, but EOTs 4 and 5 are degenerate. EOTs 6 and higher explain only small fractions of the total space–time variance. For consistency with Part I of this study, we analyze EOTs 1, 2 and 3 for both summer and winter.

Connections between regional rainfall and large-scale atmospheric circulation patterns are established by linearly regressing atmospheric data sets onto each EOT timeseries. All computations are performed on 26 years (1982–2007) of pentad data after removing the pentad climatology. Regressions show the change associated with a one standard deviation increase in the EOT timeseries, but all discussions hold for negative anomalies in the EOT timeseries, with patterns of opposite signs. We use Spearman's rank correlations because the rainfall data are not normally distributed.

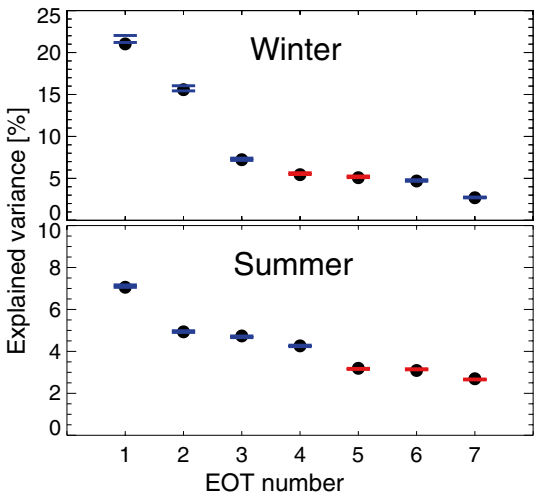

Fig. 1 Fraction of total space–time variance explained by the seven leading EOTs for winter and summer. Error bars are computed by omitting 1 year at a time and are shown as horizontal bars. Red bars denote EOTs that are 'degenerate' (i.e. not distinctly different from all other EOTs), following the procedure outlined in Sect. 2.1

2.2 Precipitation data

Daily precipitation over China is obtained from the Asian Precipitation—Highly-Resolved Observational Data Integration Towards Evaluation (APHRODITE; Yatagai et al. 2012) data set, with a resolution of 0.5° × 0.5°. Please refer to Part I for a description of this data set. We compute pentad precipitation timeseries for 26 years of winter (NDJFMA) and summer (MJJASO) by averaging over 5-day intervals starting on 1 Nov 1981 for winter and 1 May 1982 for summer, such that each season consists of 36 pentads. These years are chosen to match the record of BSISO index data (1981 onwards) made available by the International Pacific Research Center at the University of Hawaii. Furthermore, we remove the climatological seasonal cycle by subtracting the 26-year mean from each pentad. These two choices focus the analysis on a subseasonal timescale.

2.3 Atmospheric and oceanic data

To investigate the influence of the atmospheric circulation on regional precipitation patterns, the following fields from the European Centre for Medium-Range Weather Forecasting Interim global reanalysis (ERA-Interim; Dee et al. 2011) are regressed against EOT timeseries, using data for 1981–2007 at 0.7° × 0.7° resolution: horizontal wind and geopotential height at 850, 500, and 200 hPa, horizontal wind divergence at 200 hPa, streamfunction at 500 hPa, mean sea level pressure (MSLP), 2 m air temperature, and vertically integrated moisture flux. We employ monthly means of 2.5° × 2.5° interpolated satellite-retrieved outgoing longwave radiation data (OLR; Liebmann and Smith 1996) for 1981–2007, as a proxy for convective activity.

2.4 BSISO indices

To connect regional rainfall variability to the BSISO, we compute pentad-BSISO indices from the daily BSISO indices proposed by Lee et al. (2013). Their indices are computed using multivariate Empirical Orthogonal Function (MV-EOF) analysis of normalized daily mean OLR and 850 hPa zonal wind anomalies over the Asian summer monsoon region (10°S–40°N, 40°E–160°E) from May to October in 1981–2010. The anomalies are computed by removing the mean and first three harmonics of the annual cycle, then removing the mean of the previous 120 days. Lee et al. (2013) computed the first four MV-EOF modes, which together account for 19.4% of total daily variance of the combined OLR and 850 hPa wind anomalies over the selected region. The principal component timeseries of the leading two modes define BSISO-1, and the third and fourth define BSISO-2. We compute pentad BSISO-1 and BSISO-2 amplitude and phases by first forming pentads from the four

individual normalized principal component timeseries. In a second step we compute amplitude and phase for our pentad BSISO-1 and BSISO-2. Please refer to Figs. 9 and 10 in Lee et al. (2013) for composites of OLR and 850 hPa wind during each BSISO-1 and BSISO-2 phase.

2.5 Wave activity flux computation

To diagnose the direction of wave energy propagation, we regress the perturbation stream function ψ onto a normalized EOT timeseries. We then compute the wave activity flux W from the regressed ψ and the climatological mean flow $\bar{U} = (\bar{u}(x, y), \bar{v}(x, y))$. Takaya and Nakamura (2001) derived the horizontal components for stationary Rossby waves in a zonally varying basic flow:

$$W = \frac{1}{2}|\bar{U}| \begin{pmatrix} \bar{u}\left(\psi_x^2 - \psi\psi_{xx}\right) + \bar{v}\left(\psi_x\psi_y - \psi\psi_{xy}\right) \\ \bar{u}\left(\psi_x\psi_y - \psi\psi_{xy}\right) + \bar{v}\left(\psi_y^2 - \psi\psi_{yy}\right) \end{pmatrix}, \quad (1)$$

where subscripts denote partial derivatives.

3 Winter results

In the following we examine the three dominant patterns of coherent intraseasonal rainfall variability during extended winter and present their associated synoptic-timescale atmospheric circulation patterns. In addition to synoptic timescales, we discuss the interannual variability of pentad rainfall in each identified region. Afterwards, we show how particularly wet and dry periods in each region are connected to China-wide daily rainfall variability.

The three leading EOTs of pentad rainfall over China during extended winter explain 21, 15 and 7% of the total space–time variance, respectively (Fig. 2). EOT 1 peaks along the Yangtze River and has significant positive correlations with most areas in China except for the far northeast, southwest and northwest. EOT 2 is centered in the southeast and exhibits a dipole pattern with areas of variability of opposite phase to the north. The third EOT also peaks along the Yangtze valley, but its base point is located further east than that of EOT 1. It is positively correlated with precipitation variability in most of northwest and north China, and negatively correlated with some regions in the southwest.

Each EOT can explain the precipitation variability in large connected areas of China. This suggests that large-scale synoptic patterns are responsible for modulating precipitation on subseasonal timescales.

3.1 Synoptic-scale circulation patterns

3.1.1 EOT 1

Figure 3 shows regressions of fields onto EOT 1 at lead times of two, one and zero (simultaneous) pentads. At a lead time of two pentads a ridge centered over western Europe is visible in the 500 hPa geopotential height field. Wave activity flux at lead times of two and one pentads indicates an eastward propagating wave pattern. At a lead time of one pentad, in addition to the ridge over western Europe, a southwest-to-northeastward tilted trough extends from northern Africa to Siberia and a ridge develops over eastern Asia. The simultaneous regression indicates that the ridge over East Asia has intensified and is now part of a zonal dipole pattern with low pressure extending from the Arabian peninsula to central China and high pressure centered over Japan.

The 200 hPa westerly jet stream weakens at 30°N and strengthens to the south and north (not shown), creating upper-level divergence over large areas of China (simultaneous regression).

There is enhanced northward moisture transport from the South China Sea into Mongolia and Russia. A second branch of anomalous moisture flux along the southern slope of the Himalayas provides southeast China with moisture. While pentad scales are too coarse to resolve

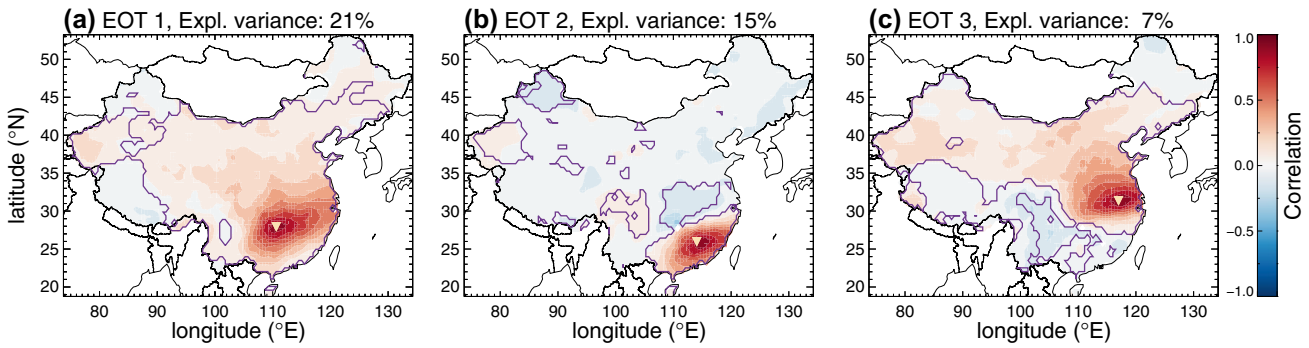

Fig. 2 Correlations of winter pentad EOT rainfall anomaly timeseries at each point with the EOT base point. The base point is marked by the orange inverted triangle. Magenta lines identify regions in which correlations are significant at the 5% level

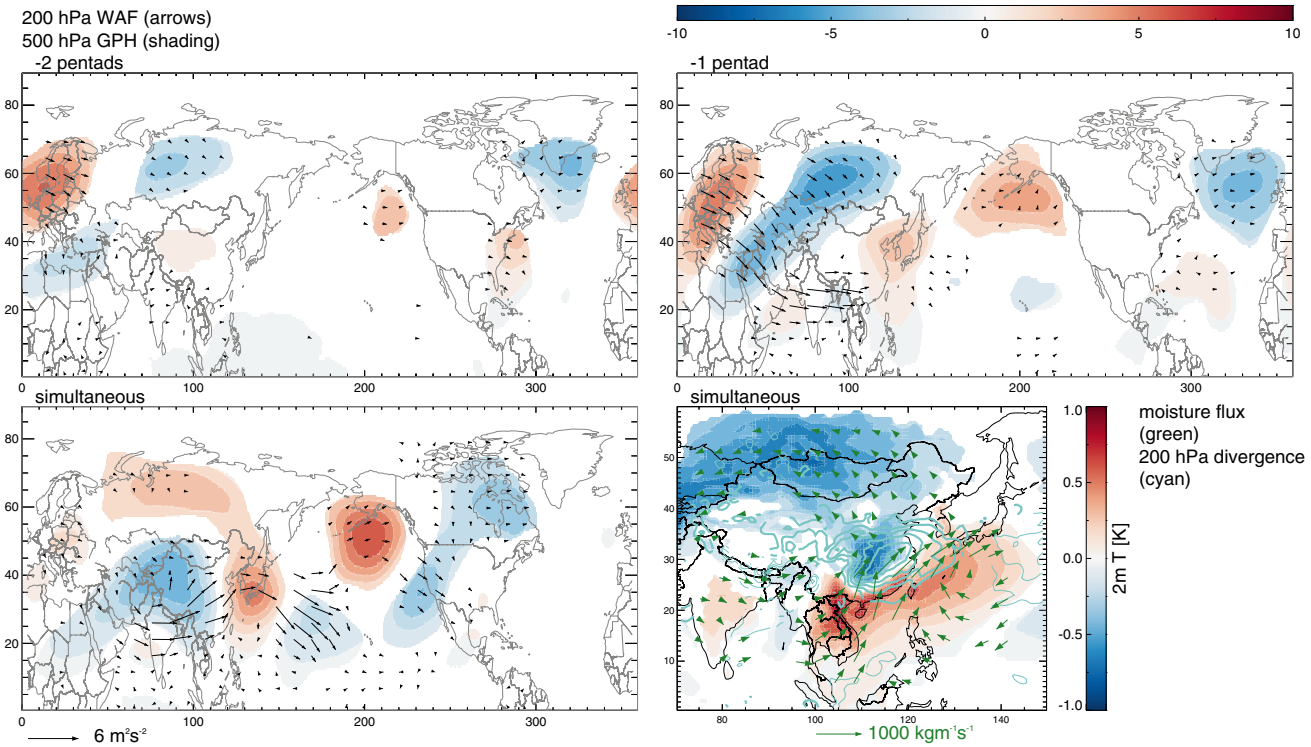

Fig. 3 Regression maps of 200 hPa wave activity flux (arrows) and 500 hPa geopotential height (shading) onto winter EOT 1 at lead times of two and one pentads (top) and simultaneous (bottom left). Bottom right: simultaneous regression of 2 m temperature (shading), moisture flux (green arrows), and 200 hPa divergence at intervals of 4.0×10^{-7} s^{-1} (cyan contours, thick: positive, thin: negative). All values shown are significant at the 10% level

frontal zones, there is a sharp temperature gradient in southern China with warm air along the south coast and cold air within and north of the Yangtze River valley, as is often the case during wintertime cold spells.

3.1.2 EOT 2

Figure 4 shows low geopotential height in the Mediterranean Sea at a lead time of one and two pentads. The 500 hPa trough extends from the eastern Mediterranean Sea to the Pacific coast of China. Wave activity flux vectors point east and suggest that the developing low pressure over Asia is related to a strengthened Mediterranean storm track. The simultaneous regression indicates that anomalously low pressure spreads across most of China. The associated cyclonic circulation transports moisture from the Bay of Bengal and the South China Sea along the southeast coast of China, where EOT 2 peaks.

Unlike EOT 1, here the 200 hPa jet is not split, but diverted southward over South Korea and Japan (not shown), such that upper-level divergence is found only over southeastern China.

3.1.3 EOT 3

The simultaneous regression in Fig. 5 shows a strong wave pattern extending from the high latitudes of northern Europe to the western Pacific. This pattern is already present at a lead time of one pentad, but with a stronger ridge over Europe and a weaker ridge over the western Pacific compared to the simultaneous regression. The ridge over Europe can be traced back to a lead time of two pentads. The simultaneous regression of moisture flux shows two pathways for moisture: northward transport from the Indian Ocean and the Pacific into southeast China, and eastward across the Tibetan Plateau.

Anomalous southwesterlies at 200 hPa (not shown) create upper-level divergence over large areas in the northern half of China. This divergence, combined with the eastward-directed branch of moisture flux, explains the large areal coverage of the EOT 3 pattern.

3.2 Variance of EOT timeseries with the seasonal cycle

In the previous section we found the large-scale circulation patterns associated with the three winter EOTs. Since

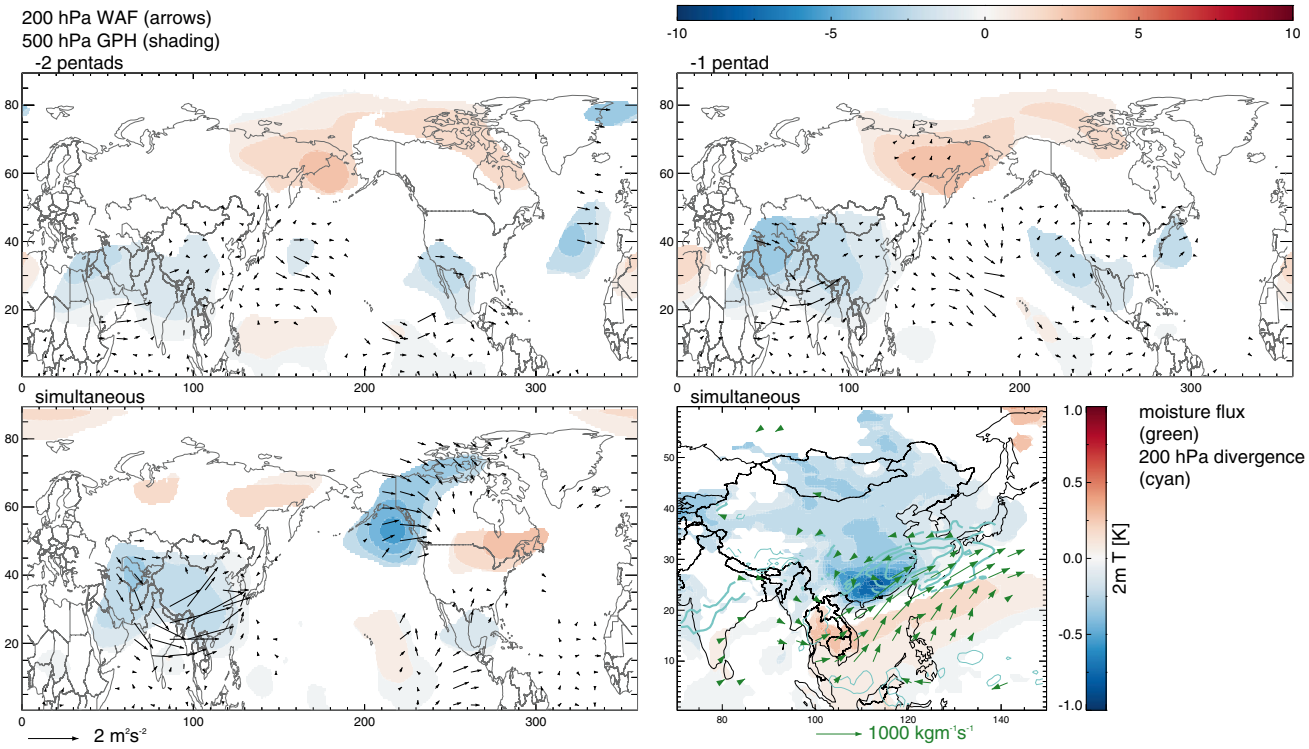

Fig. 4 As Fig. 3 but for winter EOT 2

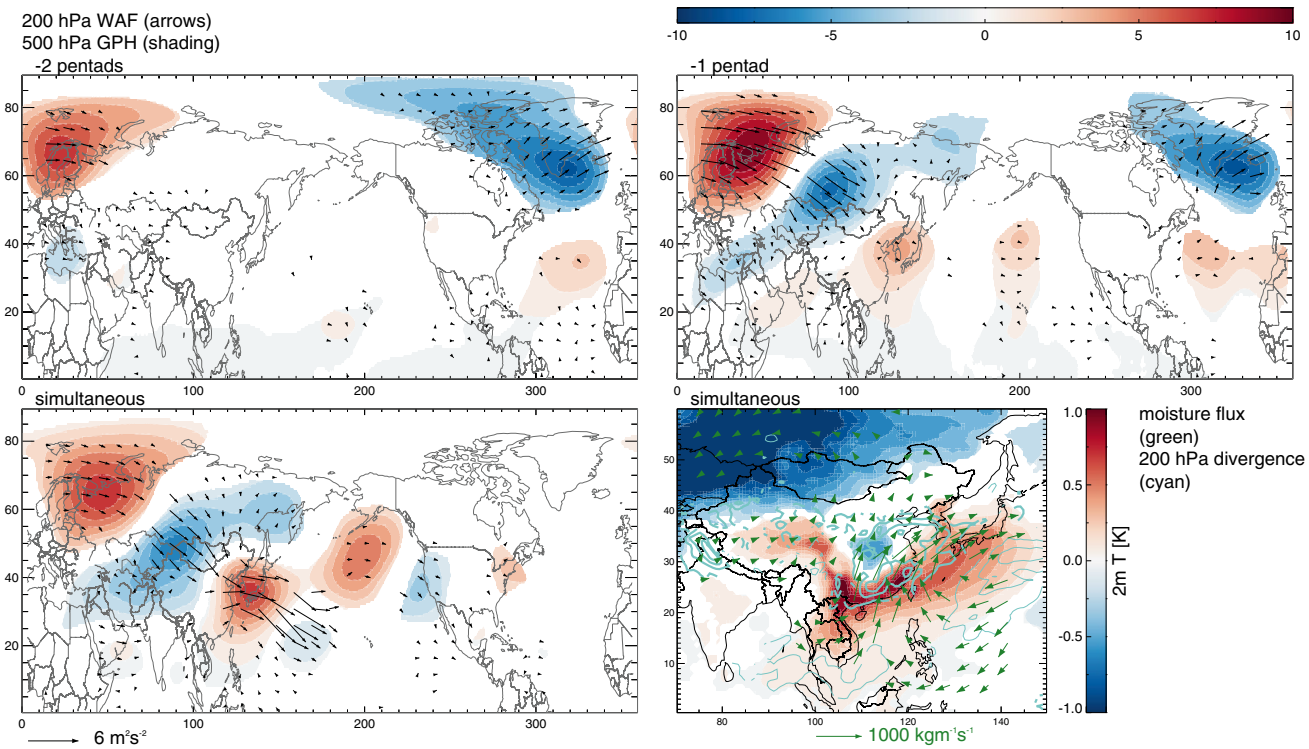

Fig. 5 As Fig. 3 but for winter EOT 3

the seasonal cycle of rainfall in China is very strong, we may reasonably suspect that the manifestations of intraseasonal variability may themselves have a seasonal cycle. In addition, driving factors of variability that impact China may also differ through the season. Therefore, we now study the seasonal cycle of the variability of each EOT timeseries. We compute the interannual standard deviation of each EOT timeseries as a function of pentad number (Fig. 6, red lines). Large standard deviations indicate that an EOT pattern tends to be active during this time of the season, i.e. particularly wet or dry pentads tend to occur during this time. Small standard deviations indicate that the precipitation anomalies associated with an EOT pattern are relatively small.

The standard deviation of EOT 1 has a minimum at six pentads, which corresponds to mid-December (Fig. 6a). Before and after this minimum, the standard deviation rises to about 4.5mm/day at the beginning of November and the end of April, respectively. The seasonal cycle of EOT standard deviation is strongly correlated (r = 0.84) with the mean seasonal cycle of precipitation in the area around the EOT 1 base point, i.e. in the central Yangtze River valley (black line). This strong relationship with the seasonal cycle is expected: during climatologically dry pentads, it is unlikely for strong rain events to occur, and therefore variance in the EOT timeseries is small.

Similar strong relationships between the mean seasonal cycle and the EOT standard deviation are obtained for EOT 2 (Fig. 6b) and EOT 3 (Fig. 6c) with correlation coefficients of 0.81 and 0.88, respectively. EOT 2, which peaks in southeast China, can be divided into a less active regime during November–January and a more active regime during February–April, during the spring rains. The seasonal cycle of EOT 3, which shows the highest spatial coherence in the eastern Yangtze valley, is similar to EOT 1.

3.3 Effects on China-wide daily rainfall

Our analysis so far has been limited to pentad precipitation variability. Here, we report how particularly wet and dry phases of each EOT modulate the characteristics of China-wide daily precipitation in terms of frequency of occurrence and intensity. For each gridpoint, we define a day as wet when total precipitation exceeds 0.5 mm. First, the climatological frequency of wet days, f_c, is computed for each season (Fig. 7i). Next, for each EOT, we select the days that fall into the wettest and driest 10% of EOT pentads, respectively, and again compute frequencies of wet days, f_{wet} and f_{dry}. The relative change in the occurrence of wet days is defined as $f_A = (f_{wet} - f_c)/(f_c) \cdot 100$ for wet phases of the EOT, and similarly $f_A = (f_{dry} - f_c)/(f_c) \cdot 100$ for dry phases. Maps of f_A are shown in the panels labeled 'Frequency' in Fig. 7. All changes shown are statistically significant at the 5% level, according to a two-tailed binomial test.

In addition to changes in the frequency of wet days, we also examine changes in precipitation intensity. The climatological precipitation intensity I_c is defined as the average amount of rainfall on wet days (Fig. 7j). Similar to the procedure above, for each EOT, I_{wet} and I_{dry} are defined as the average amount of rainfall on wet days that fall into the wettest and driest 10% of EOT pentads. The changes in intensities $I_A = (I_{wet} - I_c)/(I_c) \times 100$ for wet phases, and $I_A = (I_{dry} - I_c)/(I_c) \times 100$ for dry phases are shown in the panels labeled 'Intensity' in Fig. 7. For I_A, statistical significance is assessed by obtaining the overall rainfall intensity distribution for wet days. A two-sided Kolmogorov–Smirnov test is performed to test whether the intensity distributions during wet and dry phases of the EOT timeseries are significantly different from the overall distribution.

In large parts of eastern China the frequencies of wet days during wet EOT 1 pentads are more than double their climatological values (Fig. 7a). The area of significant changes in frequencies agrees well with the region affected

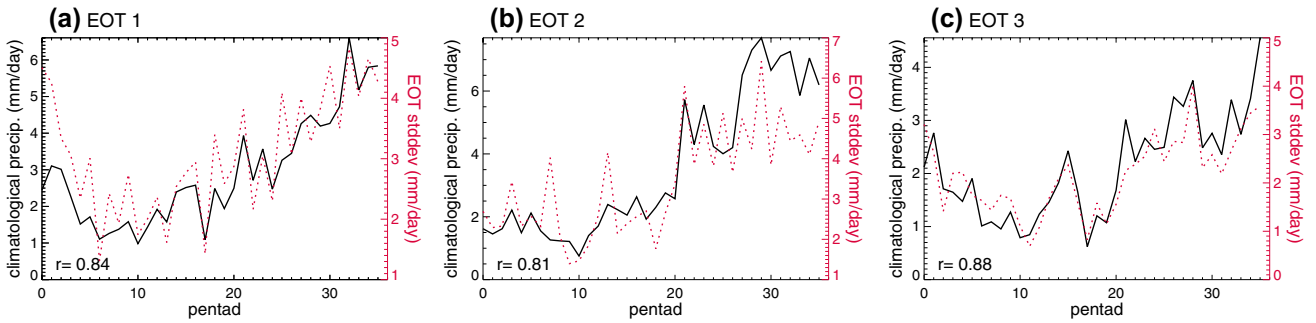

Fig. 6 Extended winter climatological pentad precipitation (black) and interannual standard deviation of the pentad EOT timeseries (red). The climatological pentad precipitation is computed by averaging over gridpoints for which correlations in Fig. 2 exceed 0.75. The Spearman's rank correlation coefficient (r) of the two timeseries is given at the bottom left of each panel. All coefficients are significant at the 1% level

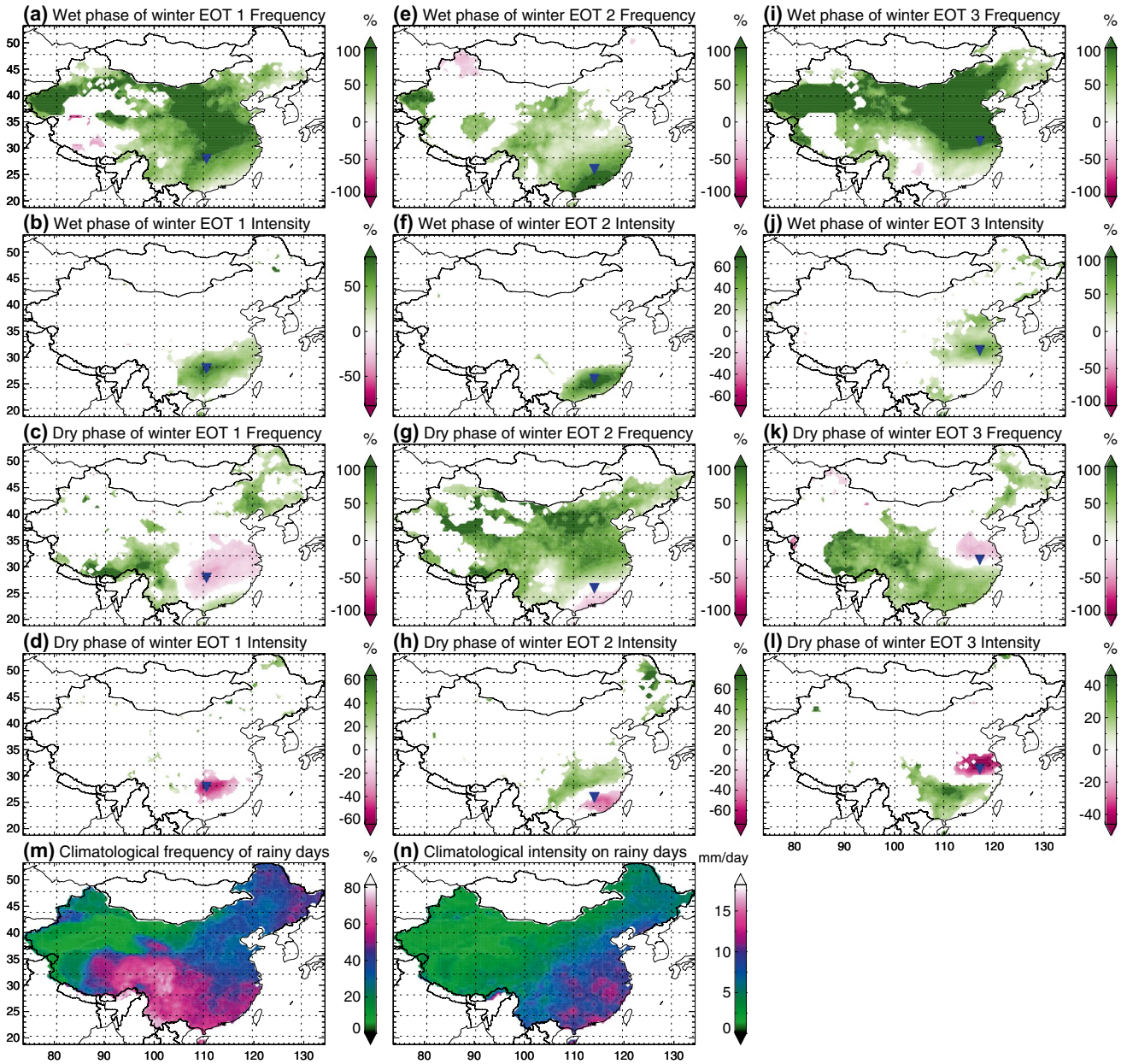

Fig. 7 Percentage change in occurrence frequency of wet days (>0.5 mm day^{-1}) for the wettest 10% (**a**, **e**, **i**) and driest 10% (**c**, **g**, **k**) of pentads for each winter EOT. Contours are shown where anomalies are significant at the 5% level based on a two-tailed binomial test. Also shown are the corresponding percentage changes in average rainfall intensities on wet days for the wettest 10% (**b**, **f**, **j**) and driest 10% (**d**, **h**, **l**) of pentads for each winter EOT. Colours are only shown were rainfall distributions differ significantly from their climatological distributions at the 5% level, according to a two-sided Kolmogorov–Smirnov test. The climatological occurrence frequencies of wet days and average rainfall intensities on wet days are shown in **m**, **n**. Please refer to the text in Sect. 3.3 for definitions and a detailed description

by the EOT (95% confidence region in Fig. 2a). Meanwhile, a significant change in rainfall intensity of the order of 50% is only seen along the Yangtze River, in the region surrounding the EOT 1 base point (Fig. 7b). A change of opposite sign in intensity is found in the same region during the dry phases (Fig. 7d). Unlike the wet phases, the relative changes in frequency during the dry phases of EOT 1 can be negative and positive (Fig. 7c); there are relatively fewer wet days along the Yangtze River, but more wet days in southwest China and along the Himalayas, as well as in parts of northeast China. The asymmetry between Fig. 7a, c can be explained as follows: recall that in the wet phases of EOT 1, i.e. the positive phase, the anomalous moisture flux is directed eastward along the

Himalayas and across southeast China into the Yangtze valley, as well as northwestward from northeast China into Mongolia (Fig. 3). In the dry phases, moisture flux is in the opposite direction, such that moisture is transported into climatologically dry regions (Fig. 7i), where topography rises steeply towards the Himalayas. Therefore, moisture flux out of these regions does not make a large difference to the occurrence of wet days, which are few on average, but moisture flux into these regions can significantly increase their frequency.

For winter EOT 2, we find similarities with EOT 1: frequency changes during the wet phases (Fig. 7e) resemble the region affected by the EOT (95% confidence region in Fig. 2b), with up to 100% more wet days along the southeast coast, and 60% larger rainfall intensities around the base point (Fig. 7f). During the dry phase, the rainfall intensity is reduced by ~40% in southeast China while it increases along the Yangtze River by ~40%. Changes in wet day frequencies for the dry phases of EOT 2 (Fig. 7g) strongly resemble those for the wet phases of EOT 1 (Fig. 7a).

For EOT 3, which peaks in the eastern Yangtze River (Fig. 2c), there are large frequency changes during the wet phases (Fig. 7i), also resembling the region affected by the EOT (95% confidence region in Fig. 2c), with 50% larger rainfall intensities in central eastern China (Fig. 7j). During dry phases both occurrence and intensity are reduced along the eastern Yangtze–Huaihe river basin, and increased in southern China (Fig. 7k, l).

4 Summer results

The spatial patterns of the leading three summer subseasonal EOTs are shown in Fig. 8a–c. Much less variance is explained by the leading subseasonal EOTs in summer compared to winter. This is because summer monsoon precipitation systems have an inherently smaller spatial scale than the extratropical systems found in winter. Nevertheless, their impact on regional rainfall can be very important. Unlike the winter EOT patterns, the three summer EOT patterns are all associated with circulation anomalies in the Indian Ocean and the Western North Pacific-East Asian region. They do not have any statistically significant links to extratropical circulation anomalies and there are no significant signals at leads of 5–10 days, unlike for winter.

EOT 1 explains 7% of the total space–time variance and describes a monopole in southern China. The spatial pattern associated with EOT 2 peaks along the Yangtze River and extends from the Pacific coast into the western half of China. Variations in the opposite phase are present in the coastal region of southeastern China. EOT 3 peaks in the southeast with variations in the opposite phase in the Yangtze–Huaihe

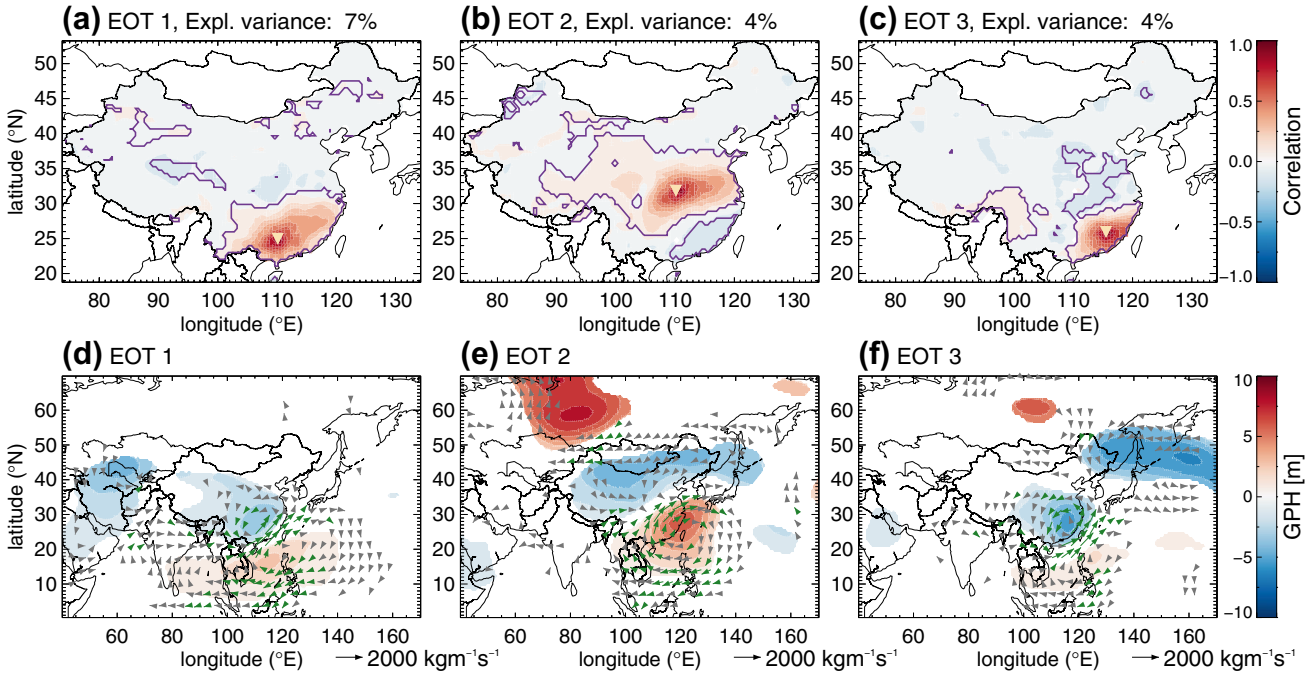

Fig. 8 Top: correlations of summer EOT rainfall anomaly timeseries at each point with the EOT base point. The base point is marked by the orange inverted triangle. Magenta lines identify regions where correlations are significant at the 5% level. Bottom: regression maps of summer 500 hPa geopotential height (GPH, shading) and moisture flux (arrows) onto the normalized summer EOT timeseries. Regression slopes are shown where correlations are significant at the 5% level. Moisture flux vectors are grey when one of the horizontal components is significant, green when both are significant at the 5% level

river basin. In the following we present evidence that all three EOTs are linked to particular phases of the BSISO (refer to Sects. 1 and 2.4 for more information and technical definitions of the BSISO indices). An examination of the seasonal cycle of the EOTs and the modulation of China-wide daily rainfall variability, as for winter, follows in Sects. 4.2 and 4.3, respectively.

4.1 Synoptic-scale circulation patterns

To associate regional rainfall variability with the BSISO, we select pentads in the 90th percentile of each summer EOT timeseries, and test whether those extremely wet pentads occur preferentially during specific phases of BSISO-1 and BSISO-2. BSISO-1 and BSISO-2 are each divided into eight phases, as shown in Fig. 9, where the inner circle with amplitudes <1 denotes a weak BSISO. Numbers show the percentages of the top 10% of summer EOT pentads that occur during each of the eight phases, including weak BSISO states. To test whether these percentages are significantly different from a distribution one might obtain randomly, we compute the climatological occurrence of each phase, and the weak states, and perform two-tailed binomial tests. In Fig. 9, red numbers indicate significantly increased percentages, and blue numbers significantly reduced percentages, using a 95% confidence level. For the following discussion, refer to Figs. 9 and 10 in Lee et al. (2013) for composites of OLR and 850 hPa wind during each BSISO-1 and BSISO-2 phase.

Furthermore, we decompose each EOT timeseries $e(t)$ into a component that is explained by the BSISO and the residual, i.e. $e(t) = e_{BSISO}(t) + e_{res}(t)$. The BSISO-related timeseries is found by multiple linear regression onto the four BSISO principle component timeseries, i.e. $e_{BSISO}(t) = a_0 + a_1 PC_1(t) + a_2 PC_2(t) + a_3 PC_3(t) + a_4 PC_4(t)$, where a_i are constants. Figure 10 shows regressions of OLR and 850 hPa wind onto $e_{BSISO}(t)$ and $e_{res}(t)$ for each EOT.

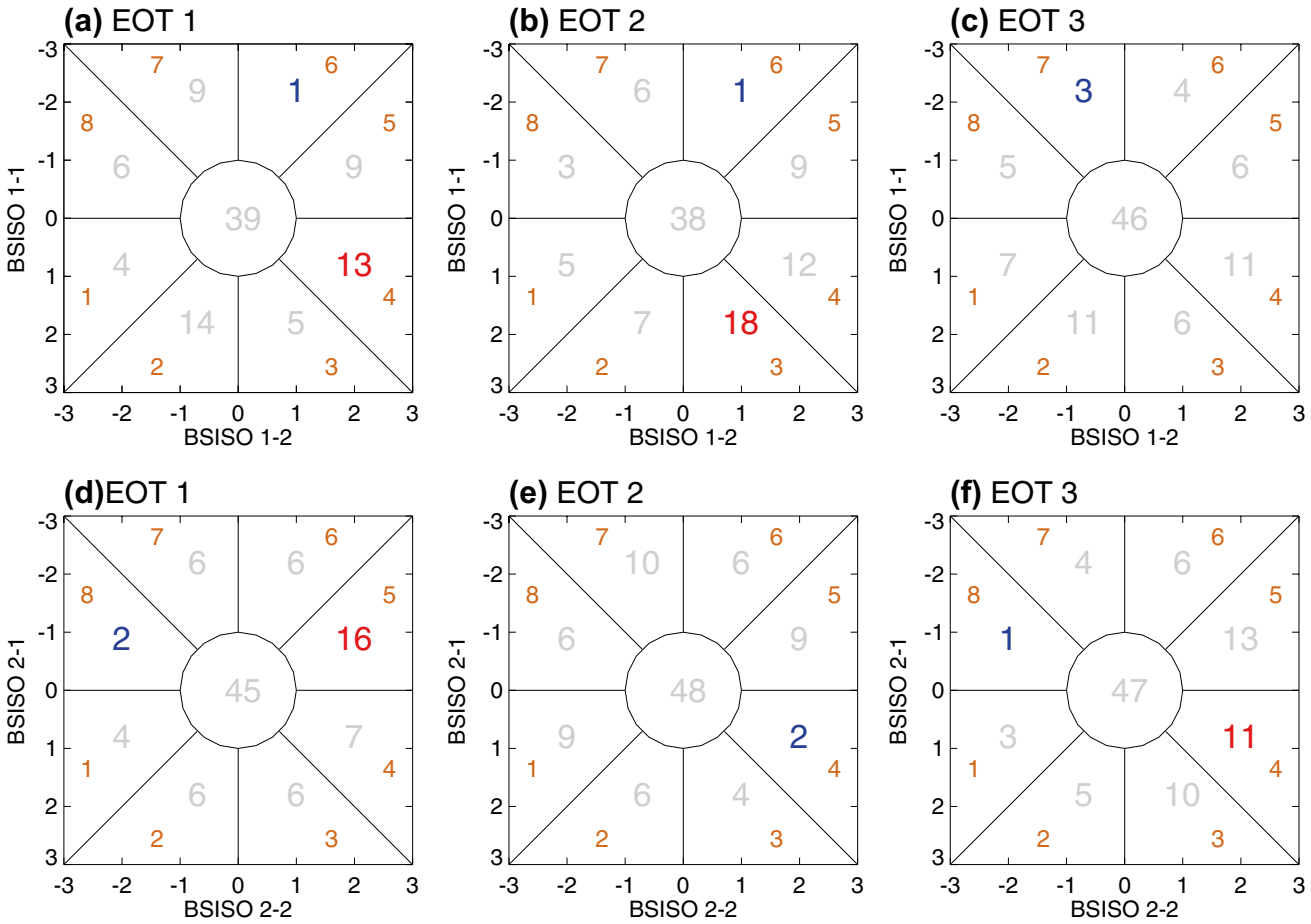

Fig. 9 Numbers show the percentages of the wettest 10% of EOT pentads that occur during the eight phases of BSISO-1 (top) and BSISO-2 (bottom). The number in the center indicates weak events, i.e. BSISO phases with amplitudes <1. Phases 1–8 are labeled in brown. Red numbers indicate significantly increased percentages, blue significantly reduced percentages, using a 95% confidence level. Please refer to the text for more details

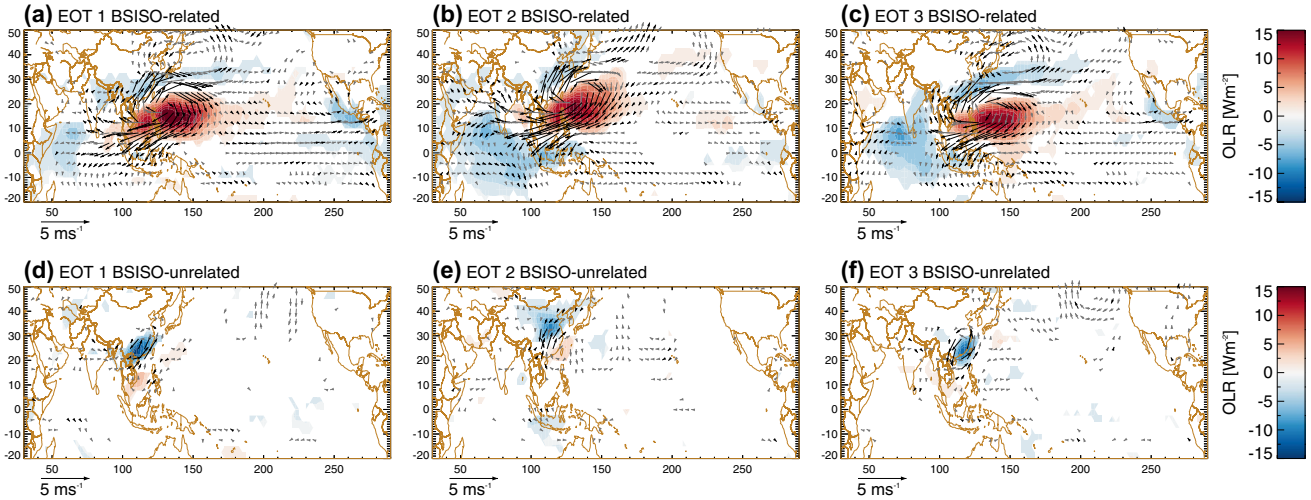

Fig. 10 Regression maps of OLR and 850 hPa wind onto the BSISO-related (**a**, **b**, **d**) and residual (**d**, **e**, **f**) components of each EOT time-series. Arrows are black when both components are statistically significant at the 5% level, grey when one component is statistically significant at the 5% level. Please refer to the text for a definition of the BSISO-related and residual components

4.1.1 EOT 1

Figure 9 indicates that events in the 90th percentile of EOT 1 occur preferentially during phase 4 of BSISO-1 and phase 5 of BSISO-2. BSISO-1 phase 4 describes the northward propagation of convection from the tropical Indian Ocean into the Bay of Bengal with a simultaneous eastward propagation of convection across the Maritime Continent into the tropical western Pacific. During this phase a lack of convection and an anticyclonic circulation are situated southeast of China; winds on the northwestern side of the anticyclonic circulation advect moisture into southern China (Fig. 10a).

Phase 5 of BSISO-2 describes a southwest to northeast orientated band of convection propagating northwestward from the South China Sea and the Indian Ocean over East Asia. The regression of 500 hPa geopotential height and moisture flux (Fig. 8d) onto EOT 1 is consistent with a frontal zone along the southeastern coast of China. The band of southwesterly moisture flux stretching from India to southern Japan resembles the lower-tropospheric winds associated with BSISO-2 phase 5 that can also be seen in Fig. 10a.

EOT 1 anomalies that are not explained by the BSISO are positively correlated with OLR anomalies in the South China Sea (Fig. 10d).

4.1.2 EOT 2

A high pressure system centered over Taiwan transports moisture from the South China Sea northwards (Fig. 8e). Strong positive events are associated with BSISO-1 phase 3, which is consistent with the southwesterly lower-tropospheric flow in southeastern China, offshore winds near 30°N and easterlies over the Philippines. In addition, there is significant eastward moisture flux across Bangladesh and the Tibetan Plateau. Figure 10b closely resembles the characteristic wind and OLR patterns associated with this phase (e.g., Lee et al. 2013), including circulation and OLR anomalies over the Indian Ocean.

EOT 2 anomalies that are not explained by the BSISO are positively correlated with OLR anomalies over Taiwan (Fig. 10e).

4.1.3 EOT 3

Low pressure and a cyclonic circulation can be seen over the coastal area of southeast China (Figs. 8f, 10c). Moisture is also transported along the southern slopes of the Himalayas. Another area of positive covariability is located where this eastward flux and the southward flux associated with the cyclonic feature converge over southeastern China. 11% of events in the 90th percentile of EOT 3 occur during BSISO-2 phase 4. This phase is similar to BSISO-2 phase 5, described above, but with convective anomalies in the western Pacific shifted slightly southward (Fig. 10c).

EOT 3 anomalies that are not explained by the BSISO are positively correlated with a local cyclonic anomaly over southeastern China (Fig. 10e) that is consistent with the cyclonic circulation in Fig. 8f.

We conclude that the BSISO can explain the large-scale circulation and convection anomalies associated with all summer EOTs. The residual anomalies (i.e., the components not related to the BSISO) do not point to large-scale teleconnections, but are local variations in atmospheric convection.

4.2 Variance of EOT timeseries with the seasonal cycle

Figure 11 displays the same information as Fig. 6, but for summer. Like in winter, the standard deviation of the EOT timeseries follows the seasonal cycle of total precipitation. The seasonal evolution of precipitation is primarily shaped by the onset and duration of the summer monsoon (Lau and Yang 1997). The northward-propagating monsoon front first reaches South China in late May, causing the peak in mean precipitation in early summer (Fig. 11a). Its arrival in the Yangtze–Huaihe river basin during June and July can be seen in Fig. 11b as a peak in midsummer. The seasonal cycle in the peak region of EOT 3, the southeast coast, has a monsoon onset signature in May and June with a second small peak in August. The monsoon onset signatures in the seasonal cycle for peak areas of EOT 1 and EOT 3 are consistent with our findings in Sect. 4.1, where EOT 1 and EOT 3 were connected to indices for the pre-monsoon and onset component of the BSISO, namely BSISO-2 phases 5 and 4, respectively.

4.3 Effects on China-wide daily rainfall

Using the same definitions as for winter (Sect. 3.3), we examine the influence of wet and dry EOT phases on the frequency and intensity of wet days (>0.5 mm/day) for summer. For all three extended summer EOTs and in relatively small regions around their base points, wet EOT phases increase the intensity of precipitation on wet days, and dry EOT phases decrease the intensity in similar regions (Fig. 12b, f, j and d, h, l, respectively). Reductions of precipitation intensity in the EOT peak regions are of the order of 40% and increases are of the order of 60% for all EOTs. Unlike in winter, changes in occurrence frequencies are seen in similar areas for wet and dry phases (Fig. 12a, c, e, g and i, k respectively). Furthermore their spatial distribution and magnitudes resemble the changes in intensity. Frequency changes in remote regions do exist in summer, but are small compared to winter and affect mostly climatologically very dry regions.

5 Discussion

The method used in this study identifies the spatial point that best explains the variability in area-averaged precipitation (or in area-averaged residual precipitation for higher orders) over China. All identified patterns peak in the eastern part of the country because these areas have the greatest mean precipitation, and precipitation variability, and dominate the area-averaged rainfall and its variability. Covariability in the western part of China is small. This implies that different processes are responsible for subseasonal precipitation variability in the west than in the east. Furthermore, EOT spatial patterns are dominated by positive correlations due to the high contributions of variance from gridpoints in the region surrounding the base point. Therefore, strong correlations are only expected close to the base point. Nevertheless, by studying how the frequency of wet days and the rainfall intensity on these days is modulated by wet and dry phases of each EOT, we noticed significant changes in regions that are far away from the peak regions, including the west and northeast. This is the case particularly in winter, when subseasonal rainfall variability is associated with synoptic-scale midlatitude disturbances. Furthermore, results suggest that regional high correlations of rainfall anomaly timeseries with EOT timeseries in the vicinity of the EOT base points are due to a coherent modulation of the frequency of wet days and the intensity of rainfall on these days. Smaller correlations in remote areas, on the other hand, appear to be mainly due to coherent changes in the occurrence of wet days, not to changes in intensity. In summer, changes in daily rainfall are mainly found in regions surrounding the base points. This is consistent with smaller percentages of

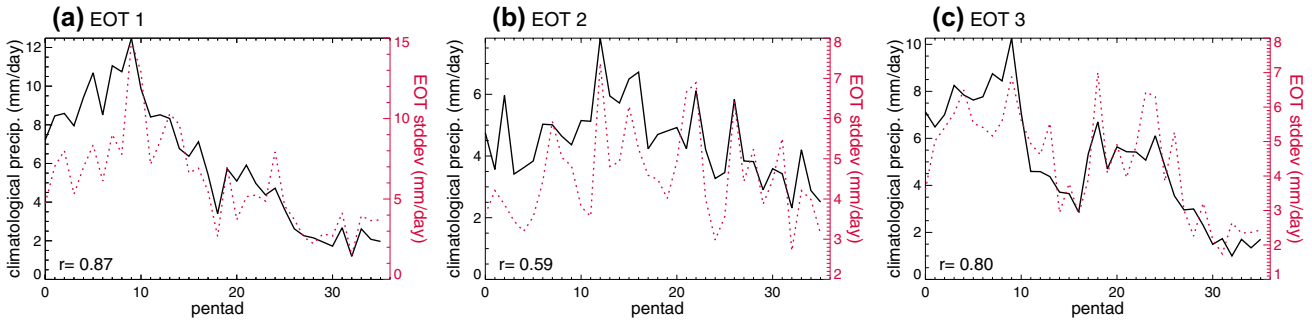

Fig. 11 Extended summer climatological pentad precipitation (black) and interannual standard deviation of the pentad EOT timeseries (red). The climatological pentad precipitation is computed by averaging over gridpoints for which correlations in Fig. 8 exceed 0.75. The Spearman's rank correlation coefficient (r) of the two timeseries is given at the bottom left of each panel. All coefficients are significant at the 1% level

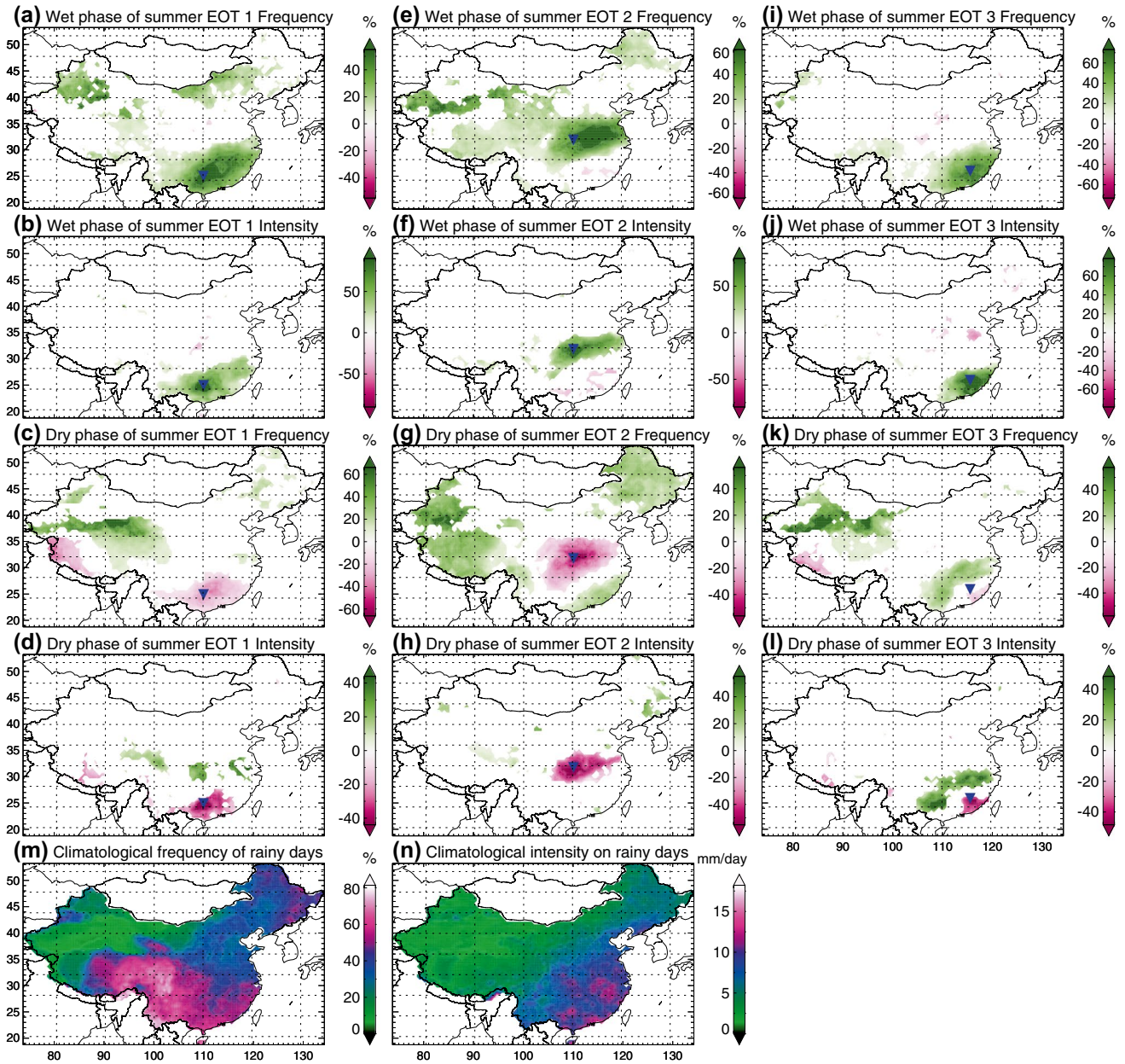

Fig. 12 Percentage change in occurrence frequency of wet days (>0.5 mm day^{-1}) for the wettest 10% (**a**, **e**, **i**) and driest 10% (**c**, **g**, **k**) of pentads for each summer EOT. Contours are shown where anomalies are significant at the 5% level based on a two-tailed binomial test. Also shown are the corresponding percentage changes in average rainfall intensities on wet days for the wettest 10% (**b**, **f**, **j**) and driest 10% (**d**, **h**, **l**) of pentads for each summer EOT. Colours are only shown were rainfall distributions differ significantly from their climatological distributions at the 5% level, according to a two-sided Kolmogorov–Smirnov test. The climatological occurrence frequencies of wet days and average rainfall intensities on wet days are shown in **m**, **n**. Please refer to the text in Sect. 3.3 for definitions and a detailed description

total explained space–time variance for the summer patterns. Summer monsoon precipitation systems have an inherently smaller spatial scale than the extratropical systems found in winter.

The peak region of winter EOT 2 shows overlap with the area in southeast China where Yao et al. (2015) showed pentad rainfall during extended winter to be affected by the MJO (their Fig. 4). They analyzed station data from 1979 to 2012 and found that 4–10% of the temporal variance in rainfall variability within the peak region of our EOT 2 could be explained by the MJO. We computed the same phase diagrams as shown in Fig. 9 for the BSISO, but for winter EOT 2 and using the MJO index of Wheeler and Hendon (2004). We could not find any evidence for an influence of

the MJO on EOT 2 (not shown). We do not expect to find a statistically significant relationship with the MJO, because the evolution of atmospheric pressure and circulation associated with EOT 2 (Fig. 4) is associated with extratropical circulation anomalies that are largely independent of the MJO. In our EOT analysis, for both winter and summer, we have considered teleconnections from the tropics to China. For the winter EOTs, no connections to tropical or sub-tropical circulation anomalies were found. This indicates that the tropics are relatively less important than the extra-tropics in winter for intraseasonal precipitation over China.

Our study provides information about regions in which subseasonal precipitation varies strongly and coherently. This information, plus the knowledge of how daily rainfall frequencies and intensities across all of China are modulated by each EOT pattern, may be useful for understanding and managing the risk of flooding. In Sect. 3.1 we were able to trace precursors of relevant large-scale circulation patterns back to lead times of ten days. Analyzing longer leads in time did not produce any physically consistent or statistically significant features. One possible reason for this limitation is that the atmospheric states found for a lead time of two pentads could result from a variety of pathways. Nevertheless, lead times of two pentads can be very valuable for forecasting precipitation. Other studies have encountered similar limits: in their EOF analysis of wintertime pentad precipitation over China, Yao et al. (2015) identified a cold-air outbreak in East Asia associated with a wave train from the North Atlantic. This wave train (their Fig. 11) resembles our Fig. 5. They further attempted to trace the wave train back to an origin in the lower stratosphere over the North Atlantic, as was suggested by Park et al. (2014), but could not find sufficient evidence. We could not identify a stratospheric origin either. Studies that investigated the origin of cold surges over East Asia report antecedent large-scale wave trains over the Eurasian continent (Takaya and Nakamura 2005; Jeong et al. 2006; Park et al. 2008, 2011). Their wave patterns do not resemble the patterns we report here, but appear at higher latitudes. This may be expected because the strength of the Siberian high was an important factor in these studies. To our knowledge, the dynamic evolutions shown in Figs. 3 and 4, and the specific evolution in Fig. 5 and its connection to intraseasonal rainfall variability, have not been previously reported.

EOT timeseries are constrained to be orthogonal only in time, which facilitates the interpretation of associated atmospheric circulation patterns: in studying the first-order impacts of dynamical mechanisms on precipitation variability, we can focus on specific locations, i.e. the EOT base points. Our results are suitable for assessing global climate models and numerical weather prediction models. The atmospheric circulation patterns, especially in winter, are complex in their evolution; it would be interesting to investigate how well numerical models can reproduce them, and their effects on East Asian precipitation. We have emphasized the importance of several factors, including upper-atmosphere dynamics, storm tracks, topography, and moisture flux, which act together and are coupled to one another to produce these patterns. These factors encompass a variety of spatial and temporal scales. Our analysis techniques could be used to test the sensitivity of model representations of East Asian precipitation variability to horizontal and vertical grid resolution and atmosphere-ocean coupling, for example. This also applies to our results for summer. It remains challenging for numerical models to correctly capture the BSISO and the seasonal cycle of precipitation, which we showed modulates the EOT timeseries substantially [see Fang et al. (2016) and references therein].

We showed that intraseasonal rainfall variability in winter is associated with extratropical wave trains; rainfall variability in summer is associated with the BSISO. In part I of this study, which examined rainfall variability on interannual timescales, we showed that variability in December–February seasonal mean rainfall in some regions is also influenced by ENSO; June–August seasonal mean rainfall in some regions is also associated with extratropical waves. Furthermore, the patterns of intraseasonal precipitation variability are different from the patterns of interannual precipitation variability. These differences in the manifestations of interannual and intraseasonal precipitation variability in China indicate that interannual variability cannot be explained as the integral of intraseasonal variability. This is indeed not expected: ENSO, for example, varies on timescales of multiple years; it is not expected to have a strong influence on five-to-five day precipitation variability. In turn, intraseasonal positive and negative rainfall anomalies can cancel each other within one season and may therefore not project onto interannual variability.

6 Summary

Using Empirical Orthogonal Teleconnection analysis, we identified the dominant regions of coherent intraseasonal precipitation variability in China, and connected that variability to synoptic-scale circulation patterns. We confirmed strong links between summer subseasonal precipitation variability and the BSISO, and discovered new connections between winter precipitation variability and extratropical synoptic patterns. Together with Part I, which focuses on interannual variability of seasonal precipitation, our study applies the same technique to examine the causes of interannual and intraseasonal precipitation variability in China across all seasons. The objectively identified patterns of regional rainfall variability are tied to specific locations in China. This facilitates their physical interpretation and is

potentially useful for understanding hydrological risks. A summary of the main results follows.

Together, the first 3 EOTs in extended winter explain 43% of the total space–time variance in area-averaged pentad rainfall over China (Fig. 2). The dominant region of precipitation variability is centered along the Yangtze River, but coherent variability exists in most areas of China. This precipitation variability is associated with a wave train of Atlantic origin that can be identified two pentads in advance (Fig. 3). During wet phases the frequency of days with precipitation >0.5 mm is more than doubled in large parts of eastern China (Fig. 7a). Along the Yangtze valley, precipitation intensity on days with rainfall >0.5 mm increases by 50% during wet phases, and decreases by 50% during dry phases (Fig. 7b, d).

Increased winter precipitation along the coast of southeast China is associated with an intensifying depression over Asia that is connected to the Mediterranean storm track (Fig. 4). During wet phases, twice as many wet days are seen along the southeast coast and 60% larger rainfall intensities are found in southeast China. During dry phases, rainfall intensities in southeast China are reduced by ~40% and increased by ~40% along the Yangtze River (Fig. 7e–h).

Most areas of northwest and north China show coherent winter subseasonal precipitation variability with the Yangtze valley, while some regions in the southwest tend to be dry when there is increased rainfall in the Yangtze valley, and wet when the Yangtze valley experiences reduced rainfall. This variability is associated with a wave train that can be traced back to a strong ridge over northern Europe two pentads in advance (Fig. 5).

As expected, the frequency of particularly wet or dry consecutive days in regions that dominate winter precipitation variability is strongly connected to the seasonal cycle of precipitation in those regions. In winter, particularly dry or wet events occur at the beginning of November and in late winter and early spring (Fig. 6).

The explained space–time variance in summer is much smaller than in winter because of the inherently smaller scale of tropical systems compared to the large-scale drivers that we found for winter (Fig. 8a–c). Summer subseasonal rainfall variability in southern China is associated with BSISO-1 phase 4 and BSISO-2 phase 5 (Fig. 9a, d).

Anomalously wet or dry conditions along the Yangtze River with anomalously dry or wet conditions along the southeast coast, respectively, are connected to BSISO-1 phase 3 (Fig. 9b).

Rainfall variability in the southeast is associated with BSISO-2 phase 4, while variability of opposite phase is found along the Yangtze River (Fig. 9c).

As in winter, the occurrence of extremely wet or dry events is related to the seasonal cycle of precipitation (Fig. 11). In contrast to winter, the seasonal cycle of precipitation in summer varies substantially between the dominant patterns of rainfall variability. This is due to the propagation of the monsoon front. Unlike in winter, changes in occurrence frequencies and rainfall intensities are confined to smaller areas. This is due to the inherently smaller scale of tropical weather systems. Increases of occurrence frequencies and rainfall intensities during wet EOT phases are of the order of 60% for all EOTs; reductions during dry phases are of the order of 20–40% (Fig. 12).

The results presented here indicate that the leading modes of intraseasonal variability of precipitation in China have statistically significant precursors about two pentads in advance. In winter preceding signals have their origins in the extratropics, often over Europe and the North Atlantic. In summer, the BSISO plays an important role. The links between weather patterns, precursors, their seasonal cycle and their effects on local and remote daily precipitation, may be valuable for predicting the risk of intense precipitation events or drought, and evaluating and improving numerical weather prediction models.

Acknowledgements The authors thank the three anonymous reviewers for their constructive comments to improve the manuscript. This work and its contributors (Claudia Christine Stephan, Pier Luigi Vidale, Andrew Turner, Marie-Estelle Demory and Liang Guo) were supported by the UK-China Research and Innovation Partnership Fund through the Met Office Climate Science for Service Partnership (CSSP) China as part of the Newton Fund. Nicholas Klingaman was supported by an Independent Research Fellowship from the UK Natural Environment Research Council (NE/L010976/1). APHRODITE data are available from http://www.chikyu.ac.jp/precip/. OLR data is provided by the NOAA/OAR/ESRL PSD, Boulder, Colorado, USA, at http://www.esrl.noaa.gov/psd/. BSISO indices are made available by the International Pacific Research Center at the University of Hawaii at http://iprc.soest.hawaii.edu/users/jylee/bsiso/. The MJO index is obtained from the Australian Bureau of Meteorology (http://www.bom.gov.au/climate/mjo/). The Rossby wave source function was computed using code from the python package windspharm v1.5.0 available at http://ajdawson.github.io/windspharm.

Open Access This article is distributed under the terms of the Creative Commons Attribution 4.0 International License (http://creativecommons.org/licenses/by/4.0/), which permits unrestricted use, distribution, and reproduction in any medium, provided you give appropriate credit to the original author(s) and the source, provide a link to the Creative Commons license, and indicate if changes were made.

References

Annamalai H, Sperber KR (2005) Regional heat sources and the active and break phases of boreal summer intraseasonal (30–50 day) variability. J Atmos Sci 62:2726–2748. doi:10.1029/2004GL020996

Barriopedro D, Gouveia CM, Trigo RM, Wang L (2012) The 2009/10 drought in China: possible causes and impacts on vegetation. J Hydrometeorol 13(4):1251–1267. doi:10.1175/JHM-D-11-074.1

Boyle JS, Chen TJ (1987) Synoptic aspects of the wintertime East Asian monsoon. In: Chang CP, Krishnamurti TN (eds) Monsoon meteorology. Oxford University Press, Oxford, pp 125–160

Chang CP (2004) East Asian monsoon. World Scientific Publishing, Toh Tuck Link

Chen TC, Chen JM (1993) The 10–20 day mode of the 1979 Indian monsoon: its relation with the time variation of monsoon rainfall. Mon Weather Rev 121:2465–2482

Chen T-C, Huang W-R, Yoon J-H (2004) Interannual variation of the East Asian cold surge activity. J Clim 34:293–305

Dee DP, Uppala SM, Simmons AJ, Berrisford P, Poli P, Kobayashi S (2011) The ERA–interim reanalysis: configuration and performance of the data assimilation system. Q J R Meteorol Soc 137:553–597

Fang Y et al (2016) High-resolution simulation of the boreal summer intraseasonal oscillation in Met Office Unified model. Q J R Meteorol Soc. doi:10.1002/qj.2927

Gao H et al. (2008) Analysis of the severe cold surge, ice-snow and frozen disasters in south China during January 2008: II. Possible climatic causes. Meteorol Mon 34:101–106 **(in Chinese)**

Gao J, Chen C, Zhou X, You L (2013) Analysis of low-frequency features on typical persistent heavy rainfall during pre-flood season in Fujian province in 2010. Adv Meteorol Sci Technol 3:39–45 **(in Chinese)**

Gu L, Wei K, Huang RH (2008) Severe disaster of blizzard, freezing rain and low temperature in January 2008 in China and its association with the anomalies of East Asian monsoon system. Clim Environ Res 13:405–418 **(in Chinese)**

He J, Lin H, Wu Z (2011) Another look at influences of the Madden–Julian oscillation on the wintertime East Asian weather. J Geophys Res 116:D03109. doi:10.1029/2010JD014787

Hong S (2004) Comparison of heavy rainfall mechanisms in Korea and the central US. J Meteorol Soc Jpn 82:1469–1479. doi:10.2151/jmsj.2004.1469

Hsu P-C, Lee J-Y, Ha K-J (2016) Influence of boreal summer intraseasonal oscillation on rainfall extremes in southern China. Int J Climatol 36:1403–1412. doi:10.1002/joc.4433

Huang RH, Xu YH, Wang PF, Zhou LT (1998) The features of the catastrophic flood over the Changjiang river basin during the summer of 1998 and cause exploration. Clim Environ Res 3:300–313 **(in Chinese)**

Huang RH, Zhou LT (2002) Research on the characteristics, formation mechanism and prediction of severe climatic disasters in China. J Nat Disasters 1:910–942 **(in Chinese)**

Jeong J, Ho C (2005) Changes in occurrence of cold surges over East Asia in association with Arctic Oscillation. Geophys Res Lett 32:L14704. doi:10.1029/2005GL023024

Jeong J-H, Ho C-H, Kim B-M, Kwon W-T (2005) Influence of the Madden–Julian Oscillation on wintertime surface air temperature and cold surges in East Asia. J Geophys Res 110:D11104. doi:10.1029/2004JD005408

Jeong JH, Kim BM, Ho CH, Chen D, Lim GH (2006) Stratospheric origin of cold surge occurrence in East Asia. Geophys Res Lett 33:L14710. doi:10.1029/2006GL026607

Jia X, Chen L, Ren F, Li C (2011) Impacts of the MJO on winter rainfall and circulation in China. Adv Atmos Sci 28:521–533. doi:10.1007/s00376-010-9118-z

Kajikawa Y, Yasunari T (2005) Interannual variability of the 10–25- and 30–60-day variation over the South China Sea during boreal summer. Geophys Res Lett 32:L04710. doi:10.1029/2004GL021836

Kemball-Cook S, Wang B (2001) Equatorial waves and air–sea interaction in the boreal summer intraseasonal oscillation. J Clim 14:2923–2942

Kim KY, Roh JW, Lee DK, Jhun JG (2010) Physical mechanisms of the seasonal, subseasonal, and high-frequency variability in the seasonal cycle of summer precipitation in Korea. J Geophys Res Atmos 115:D14110. doi:10.1029/2009JD013561

King AD, Klingaman NP, Alexander LV, Donat MG, Jourdain NC, Maher P (2014) Extreme rainfall variability in Australia: patterns, drivers, and predictability. J Clim 27:6035–6050. doi:10.1175/JCLI-D-13-00715.1

Klingaman NP, Woolnough SJ, Syktus J (2013) On the drivers of interannual and decadal rainfall variability in Queensland, Australia. Int J Climatol 33:2413–2430. doi:10.1002/joc.3593

Krishnamurti TN, Subramanian D (1982) The 30–50 day mode at 850 mb during MONEX. J Atmos Sci 39:2088–2095

Lau KM, Yang S (1997) Climatology and interannual variability of the southeast Asian summer monsoon. Adv Atmos Sci 14:141–162. doi:10.1007/s00376-997-0016-y

Lau N-C, Lau K-M (1984) The structure and energetics of midlatitude disturbances accompanying cold-air outbreaks over East Asia. Mon Weather Rev 112:1309–1327

Lau WKM, Chan PH (1986) Aspects of the 40–50 day oscillation during the northern summer as inferred from outgoing long wave radiation. Mon Weather Rev 114:1354–1367

Lee J-Y, Wang B, Wheeler MC, Fu X, Waliser DE, Kang I-S (2013) Real-time multivariate indices for the boreal summer intraseasonal oscillation over the Asian summer monsoon region. Clim Dyn 40:493–509. doi:10.1007/s00382-012-1544-4

Li J, Mao J, Wu G (2015) A case study of the impact of boreal summer intraseasonal oscillations on Yangtze rainfall. Clim Dyn 44:2683–2702. doi:10.1007/s00382-014-2425-9

Liebmann B, Smith CA (1996) Description of a complete (interpolated) outgoing longwave radiation dataset. Bull Am Meteorol Soc 77:1275–1277

Liu D, Yang X (2010) Mechanism responsible for the impact of Madden–Julian oscillation on the wintertime rainfall over eastern China. Sci Meteorol Sin 30:684–693

Liu HB, Yang J, Zhang DL, Wang B (2014) Roles of synoptic to quasi-biweekly disturbances in generating the summer 2003 heavy rainfall in East China. Mon Weather Rev 142:886–904

Madden RA, Julian PR (1972) Description of global-scale circulation cells in tropics with a 40–50 day period. J Atmos Sci 29:1109–1123

Mao J, Wu G (2006) Intraseasonal variations of the Yangtze rainfall and its related atmospheric circulation features during the 1991 summer. Clim Dyn 27:815. doi:10.1007/s00382-006-0164-2

Mao JY, Sun Z, Wu G-X (2010) 20–50-Day oscillation of summer Yangtze rainfall in response to intraseasonal variations in the subtropical high over the western North Pacific and South China Sea. Clim Dyn 34:747–761

Mao R, Gong DY, Yang J, Bao JD (2011) Linkage between the Arctic Oscillation and winter extreme precipitation over central-southern China. Clim Res 50:187–201. doi:10.3354/cr01041

Murakami M (1984) Analysis of deep convective activity over the western Pacific and southeast Asia. Part II: seasonal and intraseasonal variations during northern summer. J Meteorol Soc Jpn 62:88–108

Park TW, Ho CH, Deng Y (2014) A synoptic and dynamical characterization of wave-train and blocking cold surge over East Asia. Clim Dyn 43:753–770. doi:10.1007/s00382-013-1817-6

Park T-W, Ho C-H, Yang S (2011) Relationship between the Arctic Oscillation and cold surges over East Asia. J Clim 24:68–83. doi:10.1175/2010jcli3529.1

Park T-W, Jeong J-H, Ho C-H, Kim S-J (2008) Characteristics of atmospheric circulation associated with cold surge occurrences in East Asia: a case study during 2005/06 winter. Adv Atmos Sci 25:791–804. doi:10.1007/s00376-008-0791-0

Rotstayn LD, Collier MA, Dix MR, Feng Y, Gordon HB, O'Farrell SP, Smith IN, Syktus J (2010) Improved simulation of Australian climate and ENSO-related rainfall variability in a global climate model with an interactive aerosol treatment. Int J Climatol 30:1067–1088

Samel AN, Liang X-Z (2003) Understanding relationships between the 1998 Yangtze river flood and north–east Eurasian blocking. Clim Res 23:149–158. doi:10.3354/cr023149

Smith I (2004) An assessment of recent trends in Australian rainfall. Aust Meteorol Mag 53:163–73

Stephan CC, Klingaman NP, Vidale PL, Turner AG, Demory ME, Guo L (2017) A comprehensive analysis of coherent rainfall patterns in China and potential drivers. Part I: Interannual variability. Clim Dyn. doi:10.1007/s00382-017-3882-8

Takaya K, Nakamura H (2001) A formulation of phase-independent wave-activity flux for stationary and migratory quasigeostrophic eddies on a zonally varying basic flow. J Atmos Sci 57:608–627

Takaya K, Nakamura H (2005) Mechanisms of intraseasonal amplification of the cold Siberian high. J Atmos Sci 62:4423–4440

Van den Dool HM, Saha S, Johansson A (2000) Empirical orthogonal teleconnections. J Clim 13:1421–1435. doi:10.1175/1520-0442(2000)013<1421:EOT>2.0.CO;2

Wang B (2006) The Asian monsoon. Springer-Praxis Publishing, Chichester

Wang B, Webster PJ, Teng H (2005) Antecedents and self-induction of the active-break Indian summer monsoon. Geophys Res Lett 32:L04704. doi:10.1029/2004GL020996

Wang L, Gao G, Zhang Q, Sun JM, Wang ZY, Zhang Y, Zhao SS, Chen XY, Chen Y, Wang YM, Chen LJ, Gao H (2008) Analysis of the severe cold surge, ice-snow and frozen disasters in south China during January 2008: I. Climatic features and its impacts. Meteorol Mon 34:95–100 **(in Chinese)**

Wang W-C, Gong W, Wei H (2000) A regional model simulation of the 1991 severe precipitation event over the Yangtze–Huai River valley. Part I: precipitation and circulation statistics. J Clim 13:74–92. doi:10.1175/1520-0442(2000) 013

Webster PJ, Magana VO, Palmer TN (1998) Monsoon: process, predictability, and the prospects for forecast. J Geophys Res 103:14454–14510

Wen M, Yang S, Kumar A, Zhang PQ (2009) An analysis of the large-scale climate anomalies associated with the snowstorms affecting China in January 2008. Mon Weather Rev 137:1111–1131. doi:10.3354/cr023149

Wheeler MC, Hendon HH (2004) An all-season real-time multivariate MJO index: development of an index for monitoring and prediction. Mon Weather Rev 132:1917–1932. doi:10.1175/1520-0493(2004)132<1917:AARMMI>2.0.CO;2

Yang C, Zhai P (2014) Precursor circulation features for persistent extreme precipitation in Central-Eastern China. Weather Forecast 29(2):226–240. doi:10.1175/WAF-D-13-00065.1

Yang H, Li C (2003) The relation between atmospheric intraseasonal oscillation and summer severe flood and drought in the Changjiang–Huaihe river basin. Adv Atmos Sci 20:540–553

Yang J, Wang B, Wang B, Bao Q (2010) Biweekly and 21–30 day variabilities of the subtropical East Asian monsoon over the lower reach of Yangtze river basin. J Clim 23:1146–1159. doi:10.1175/2009JCLI3005.1

Yao Y, Lin H, Wu Q (2015) Subseasonal variability of precipitation in China during boreal winter. J Clim 28(16):6548–6559. doi:10.1175/JCLI-D-15-0033.1

Yasunari T (1979) Cloudiness fluctuations associated with the northern hemisphere summer monsoon. J Meteorol Soc Jpn 57:227–242

Yasunari T (1980) A quasi-stationary appearance of 30 to 40 day period in the cloudiness fluctuation during the summer monsoon over India. J Meteorol Soc Jpn 58:225–229

Yatagai A, Kamiguchi K, Arakawa O, Hamada A, Yasutomi N, Kitoh A (2012) APHRODITE: constructing a long-term daily gridded precipitation dataset for Asia based on a dense network of rain gauges. Bull Am Meteorol Soc 93:1401–1415. doi:10.1175/BAMS-D-11-00122.1

Yihui D, Chan JC (2005) The East Asian summer monsoon: an overview. Meteorol Atmos Phys 89:117–142. doi:10.1007/s00703-005-0125-z

Yun KS, Ha KJ, Ren B, Chan JCL, Jhun JG (2009) The 30–60 day oscillation in the East Asian summer monsoon and its time-dependent association with the ENSO. Tellus A 61A:565–578

Yun KS, Seo KH, Ha KJ (2010) Interdecadal change in the relationship between ENSO and the intraseasonal oscillation in East Asia. J Clim 23:3599–3612

Zhou B et al (2011) The great 2008 Chinese ice storm: Its socioeconomic–ecological impact and sustainability lessons learned. Bull Am Meteorol Soc 92:47–60. doi:10.1175/2010BAMS2857.1

Zhu CW, Nakazawa T, Li J, Chen L (2003) The 30–60 day intraseasonal oscillation over the western North Pacific Ocean and its impacts on summer flooding in China during 1998. Geophys Res Lett. doi:10.1029/2003GL017817